Pirsto, Ville; Kukkola, Jarno; Rahman, F M Mahafugur; Hinkkanen, Marko

Real-time identification of LCL filters employed with grid converters

Published in:
IEEE Transactions on Industry Applications

DOI:
10.1109/TIA.2020.3003878

Published: 01/09/2020

Document Version
Peer reviewed version

Please cite the original version:
Pirsto, V., Kukkola, J., Rahman, F. M. M., & Hinkkanen, M. (2020). Real-time identification of LCL filters employed with grid converters. *IEEE Transactions on Industry Applications*, *56*(5), 5158-5169. [9121739]. https://doi.org/10.1109/TIA.2020.3003878

Real-Time Identification of LCL Filters Employed With Grid Converters

Ville Pirsto, Jarno Kukkola, F. M. Mahafugur Rahman, *Student Member, IEEE,* and Marko Hinkkanen, *Senior Member, IEEE*

***Abstract*—This paper presents a real-time identification method for LCL filters used with three-phase grid converters. The method can be applied to identify both the inductance and capacitance values of the filter and the series resistance seen by the converter. As a side-product, an estimate of the grid inductance seen from the point of connection is also obtained. A wideband excitation signal is added to the converter voltage reference. During the excitation, converter current and converter voltage reference samples are used for identification. The samples are preprocessed in real time by removing DC biases and significant grid-frequency harmonics. Parameters of two discrete-time models are estimated at each sampling instant with a recursive estimation algorithm. Depending on the estimated model, the model parameter estimates are translated to either the resistance or the inductance and capacitance values of the system. The method can be embedded to a control system of pulse-width-modulation (PWM) based converters in a plug-in manner. Only the DC-link voltage and converter currents need to be measured. Simulation and experimental results are presented for a 12.5-kVA grid converter system to evaluate the proposed method.**

***Index Terms*—Grid converter, LCL filter, real-time identification, recursive parameter estimation.**

I. Introduction

In the last decade, the cost of producing electricity using renewable energy resources, such as wind and solar, has reduced greatly. As a result, the penetration of renewable energy sources in the electric grid has increased enormously. These renewable energy sources are connected to the grid through a converter equipped with a filter, typically of an L or LCL type. The LCL filter has gained popularity due to its higher attenuation above its resonance frequency compared to an L filter of equal magnetic volume [1]. However, the resonant modes of the LCL filter make the control of the converter more challenging. These resonant modes are typically damped with active damping methods that are implemented in the converter control systems. Many of the active damping methods require knowledge of the reactive filter parameters, e.g., [2]–[5].

Even if the nominal parameters of the LCL filter are known, manufacturing tolerances and aging phenomena cause uncertainties in the parameters. Knowledge of the reactive parameters of the LCL filter could be used for condition monitoring and fault diagnosis, e.g., tracking long-term evolution of the filter capacitances for pre-emptive maintenance [6]. Furthermore, the estimates of the reactive filter parameters could be used to improve the converter control tuning.

Closely related to the identification of an LCL filter, there are numerous methods proposed for real-time identification of the grid impedance, e.g., [7]–[13]. The identification has been carried out using Fourier analysis [7], recursive parameter estimation [8]–[10], model predictive control [11], extended Kalman filter [12], and wavelets [13]. The real-time estimates of the grid impedance can be used, e.g., for islanding detection and improving the converter control tuning.

Post-processing-based methods for identifying the LCL filter of a grid converter have been proposed in [14]–[18]. In [14]–[16], methods for identifying a discrete-time state-space model of the LCL filter are presented. However, these methods do not yield estimates of the reactive filter parameters and they are not designed for real-time identification. In [17], [18], the inductance and capacitance values of the LCL filter are identified offline using an indirect identification approach. In this approach, the converter controller needs to be changed during the identification, as it is part of the identification model.

In [19], the values of these LCL filter parameters are identified as an online batch process, yielding a single estimate of the reactive filter parameters each time the identification method is run. Despite the number of different methods proposed for real-time identification of the grid impedance, no recursive real-time identification method for the parameters of an LCL filter has yet been proposed. Furthermore, a method capable of simultaneously identifying both the LCL filter parameters and indirectly the parameters of an inductive-resistive grid has not been presented.

The benefits of a recursive approach are significant. In the batch method approach of [19], all the data used in the identification has to be collected before the estimation can be carried out. This requires a considerable amount of memory, as data spanning several grid-frequency periods is required in practice, e.g., 0.1 seconds in the case of five grid periods (50 Hz). Furthermore, iterating through the collected data requires a high number of floating-point operations, in the range of 10^4, which can take several seconds to execute as a background process of a converter [19]. To update the estimates, the whole identification routine has to be run again. The recursive approach, on the other hand, is considerably more efficient when the estimates of the filter parameters are desired on a sample-to-sample basis, e.g., for real-time tracking of changes in the filter parameters. With the recursive approach, less memory is

Conference version of this paper was presented at the 2019 IEEE Energy Conversion Congress and Exposition, Baltimore, MD, USA, Sep. 29 – Oct. 3. The work was supported by ABB Oy.

V. Pirsto, J. Kukkola, F. M. M. Rahman, and M. Hinkkanen are with the Department of Electrical Engineering and Automation, Aalto University, Espoo, Finland (e-mail: ville.pirsto@aalto.fi; jarno.kukkola@aalto.fi; f.rahman@aalto.fi; marko.hinkkanen@aalto.fi).

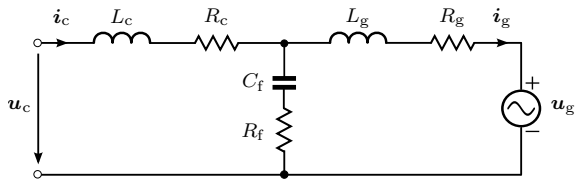

Fig. 1. Circuit model of an LCL filter connected to an inductive-resistive grid in stationary coordinates.

consumed and the number of floating-point operations required to update the estimates are several decades lower, in the range of 10^2, as will be shown in this paper.

In this paper, a real-time LCL filter identification method is proposed. The method is capable of identifying an inductive-resistive grid as a side product. The contributions of this paper, in comparison to the state-of-the-art, are:

1) The proposed method can run continuously to provide real-time estimates of the filter parameters and the grid inductance.
2) In addition to the filter parameters, a general pulse-transfer function of the system consisting of the filter and the grid is estimated in real-time. The series resistance seen by the converter is extracted from this pulse-transfer function.
3) Compared to [19], the parameter estimation of the identification model is simplified without compromising accuracy.

Additionally, the proposed recursive real-time implementation allows for distributing the computational costs over the run time of the algorithm. Despite the different characteristics of the proposed method and [19], similar estimation accuracy is maintained as both methods rely on the same prediction-error method. As compared to our earlier conference paper [20], the identification method is extended by estimating a more general pulse-transfer function of the filter and the grid, from which an estimate of the series resistance seen by the converter is extracted. Simulation and experimental results are presented for a 12.5-kVA three-phase grid converter.

II. System Model

A space-vector model for a three-phase LC or LCL filter connected between the converter and an inductive-resistive grid is shown in Fig. 1, where L_c is the converter-side inductance, C_f the filter capacitance, and L_g the grid-side inductance, consisting of the grid-side filter inductance L_fg and the grid inductance L_gr, i.e., $L_\mathrm{g} = L_\mathrm{fg} + L_\mathrm{gr}$. The resistances $R_\mathrm{c}, R_\mathrm{f}$, and R_g model the resistive losses of the filter components $L_\mathrm{c}, C_\mathrm{f}$, and L_g, respectively. If some apriori information regarding either the inductance of the grid-side filter inductor or the grid is available, these two inductances can be separated from L_g. A hold-equivalent discrete-time model of the LCL filter in stationary coordinates can be written as

$$\begin{aligned} \mathbf{x}(k+1) &= \mathbf{\Phi}\mathbf{x}(k) + \mathbf{\Gamma}_\mathrm{c}\boldsymbol{u}_\mathrm{c}(k) + \mathbf{\Gamma}_\mathrm{g}\boldsymbol{u}_\mathrm{g}(k) \\ \boldsymbol{i}_\mathrm{c}(k) &= \mathbf{C}_\mathrm{c}\mathbf{x}(k). \end{aligned} \tag{1}$$

In the above, $\mathbf{x} = [\boldsymbol{i}_\mathrm{c}, \boldsymbol{u}_\mathrm{f}, \boldsymbol{i}_\mathrm{g}]^\mathrm{T}$ is the state vector where $\boldsymbol{u}_\mathrm{f}$ is the voltage over the filter capacitor and $\mathbf{C}_\mathrm{c} = [1, 0, 0]$ (cf. Appendix A). The converter current $\boldsymbol{i}_\mathrm{c}$ can be obtained from the state-space model (1) as

$$\boldsymbol{i}_\mathrm{c}(k) = Y_\mathrm{c}(z)\boldsymbol{u}_\mathrm{c}(k) + Y_\mathrm{g}(z)\boldsymbol{u}_\mathrm{g}(k) \tag{2}$$

where the pulse-transfer operator $Y_\mathrm{c}(z)$ is given by

$$Y_\mathrm{c}(z) = \mathbf{C}_\mathrm{c}\left(z\mathbf{I} - \mathbf{\Phi}\right)^{-1}\mathbf{\Gamma}_\mathrm{c} \tag{3}$$

where z is the forward-shift operator. The pulse-transfer operator $Y_\mathrm{g}(z)$ is obtained similarly. Due to the finite computation time of the control algorithm, the converter voltage reference $\boldsymbol{u}_\mathrm{c,ref}$ is delayed by one sampling period, i.e., $\boldsymbol{u}_\mathrm{c}(k) = z^{-1}\boldsymbol{u}_\mathrm{c,ref}(k)$. Taking the computational delay into account, the pulse-transfer function from $\boldsymbol{u}_\mathrm{c,ref}$ to $\boldsymbol{i}_\mathrm{c}$ can be written as

$$Y(z) = \frac{\boldsymbol{i}_\mathrm{c}(z)}{\boldsymbol{u}_\mathrm{c,ref}(z)} = z^{-1}Y_\mathrm{c}(z). \tag{4}$$

A block diagram representation of the discrete-time LCL filter model (2) including the computational delay is shown in Fig. 2. Knowledge of the structure of $Y(z)$ is important for selecting a suitable identification model, and it can be expressed as

$$Y(z) = \frac{B(z)}{A(z)} = \frac{z^{-1}(\beta_1 z^{-1} + \beta_2 z^{-2} + \beta_3 z^{-3})}{1 + \alpha_1 z^{-1} + \alpha_2 z^{-2} + \alpha_3 z^{-3}}. \tag{5}$$

The coefficients of the above pulse-transfer function are complicated functions of the filter parameters and the sampling period T_s. If the resistances in the system are omitted, i.e., an ideal filter is considered, the number of unique coefficients in $Y(z)$ is reduced. Furthermore, the coefficients can be written using the closed-form expression of the hold-equivalent state-space model (1) of the ideal LCL filter (cf. Appendix A) as [17]

$$\begin{aligned} \alpha_1 &= -\alpha_2 = -1 - 2\cos(\omega_\mathrm{p}T_\mathrm{s}) \\ \alpha_3 &= -1 \\ \beta_1 = \beta_3 &= \frac{T_\mathrm{s} + L_\mathrm{g}\sin(\omega_\mathrm{p}T_\mathrm{s})/(\omega_\mathrm{p}L_\mathrm{c})}{L_\mathrm{c} + L_\mathrm{g}} \\ \beta_2 &= -\frac{2T_\mathrm{s}\cos(\omega_\mathrm{p}T_\mathrm{s}) + 2L_\mathrm{g}\sin(\omega_\mathrm{p}T_\mathrm{s})/(\omega_\mathrm{p}L_\mathrm{c})}{L_\mathrm{c} + L_\mathrm{g}} \end{aligned} \tag{6}$$

where ω_p is the undamped resonance frequency of the LCL filter, given by

$$\omega_\mathrm{p} = \sqrt{\frac{L_\mathrm{c} + L_\mathrm{g}}{L_\mathrm{c}C_\mathrm{f}L_\mathrm{g}}}. \tag{7}$$

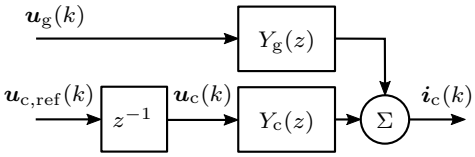

Fig. 2. Block diagram representation of the discrete-time LCL filter model including the computational delay caused by the control system.

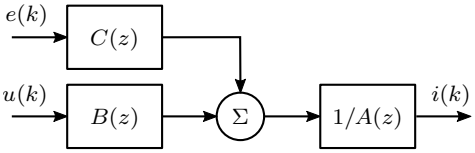

Fig. 3. ARMAX model structure.

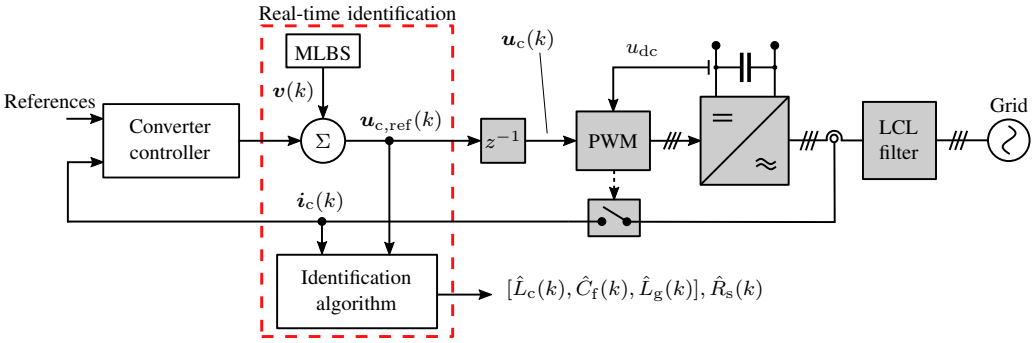

Fig. 4. Block diagram of the identification method embedded to a grid converter system.

III. Identification Model

Choice of the identification model structure is crucial for obtaining accurate results. The most common discrete-time identification model structures are divided into equation-error and output-error models [21]. Equation-error models include an error term that passes through the same denominator polynomial as the input signal. Such models correspond well to the model of an LCL filter, as both inputs $\boldsymbol{u}_{\mathrm{c,ref}}$ and $\boldsymbol{u}_{\mathrm{g}}$ pass through the same denominator polynomial $A(z)$ to $\boldsymbol{i}_{\mathrm{c}}$. Therefore, an autoregressive-moving-average (ARMAX) equation-error model, shown in Fig. 3, is used. Out of the available equation-error models, ARMAX is selected due to the flexibility it offers for modeling the error term. The discrete-time ARMAX model can be expressed as [21]

$$A(z)i(k) = B(z)u(k) + C(z)e(k) \tag{8}$$

where $i(k)$ is the preprocessed converter current $\boldsymbol{i}_{\mathrm{c}}(k)$ corresponding to the model output, $u(k)$ is the preprocessed converter voltage reference $\boldsymbol{u}_{\mathrm{c,ref}}(k)$ corresponding to the model input, and $e(k)$ represents white noise with zero mean. The grid voltage $\boldsymbol{u}_{\mathrm{g}}$ is not included in the model, as it is assumed to be unknown in order to increase the generality of the proposed method. However, this exclusion does not pose a problem since the influence of the grid voltage is effectively removed from the samples used in the identification, as will be discussed in Section IV-B.

As the structure of the LCL filter dynamics from $\boldsymbol{u}_{\mathrm{c,ref}}$ (corresponding to u) to $\boldsymbol{i}_{\mathrm{c}}$ (corresponding to i) is known [cf. (5)], the orders of the polynomials $A(z)$ and $B(z)$ are selected identical to the denominator and numerator of $Y(z)$ given in (5), respectively. For selecting the numerator polynomial $C(z)$, a parsimonious approach is adopted for the sake of generality of the model [22]. A second-order polynomial

$$C(z) = 1 + c_1 z^{-1} + c_2 z^{-2} \tag{9}$$

is employed, as it was found to yield similar results as compared to higher-order polynomials in various simulations and experiments. However, the order of $C(z)$ can be optimized for specific systems by using advanced model-order selection approaches, such as the Akaike information criterion [22].

Next, the regression models for the realistic and ideal LCL filters are presented. The realistic filter model is employed to obtain an estimate of the series resistance $\hat{R}_{\mathrm{s}} = \hat{R}_{\mathrm{c}} + \hat{R}_{\mathrm{g}}$ seen by the converter. As the reactive parameters are difficult to obtain directly from the realistic model, an ideal filter model is also considered. In the ideal filter model, the losses of the components are neglected. This allows for expressing the reactive filter parameters as functions of the estimated polynomial coefficients [cf. (24)].

A. Regression Model for the Realistic LCL Filter

The ARMAX model (8) of a realistic LCL filter (5) can be written as a regression model

$$y_{\mathrm{r}}(k) = \boldsymbol{\varphi}_{\mathrm{r}}^{\mathrm{T}}(k)\boldsymbol{\theta}_{\mathrm{r}} + e(k) \tag{10}$$

where the regressed variable is

$$y_{\mathrm{r}}(k) = i(k) \tag{11}$$

and the regressor vector $\boldsymbol{\varphi}_{\mathrm{r}}$ and the parameter vector $\boldsymbol{\theta}_{\mathrm{r}}$ are

$$\begin{aligned} \boldsymbol{\varphi}_{\mathrm{r}}(k) = [&-i(k-1), -i(k-2), -i(k-3), u(k-2), \\ &u(k-3), u(k-4), e(k-1), e(k-2)]^{\mathrm{T}} \\ \boldsymbol{\theta}_{\mathrm{r}} = [&\alpha_1, \alpha_2, \alpha_3, \beta_1, \beta_2, \beta_3, c_1, c_2]^{\mathrm{T}} \end{aligned} \tag{12}$$

respectively.

B. Regression Model for the Ideal LCL Filter

In the regression model

$$y_{\mathrm{i}}(k) = \boldsymbol{\varphi}_{\mathrm{i}}^{\mathrm{T}}(k)\boldsymbol{\theta}_{\mathrm{i}} + e(k) \tag{13}$$

of the ideal LCL filter with polynomial coefficients (6), the regressed variable is

$$y_{\mathrm{i}}(k) = i(k) - i(k-3) \tag{14}$$

and the regressor and parameter vectors are

$$\begin{aligned} \boldsymbol{\varphi}_{\mathrm{i}}(k) = [&i(k-2) - i(k-1), u(k-2) + u(k-4), \\ &u(k-3), e(k-1), e(k-2)]^{\mathrm{T}} \\ \boldsymbol{\theta}_{\mathrm{i}} = [&\alpha_1, \beta_1, \beta_2, c_1, c_2]^{\mathrm{T}} \end{aligned} \tag{15}$$

respectively. As the resistive losses of the filter are neglected, the coefficients in polynomials $A(z)$ and $B(z)$ of the identification model (8) can be related to the parameters of the LCL filter through (6).

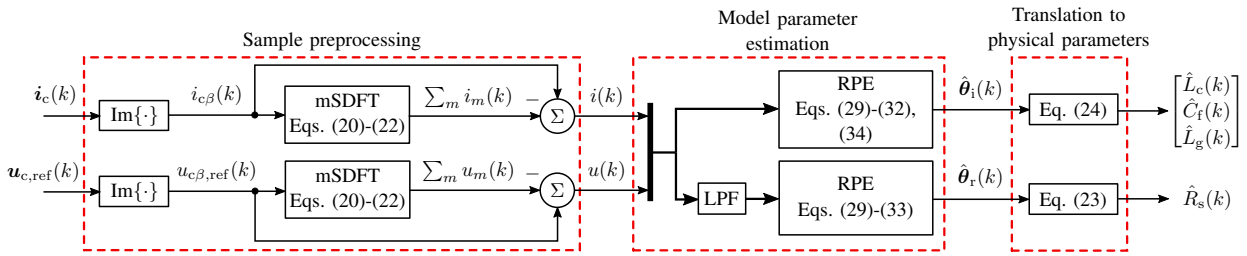

Fig. 5. Block diagram of the proposed identification method. LPF denotes a low-pass filter.

IV. Identification Method

A block diagram of the proposed identification method embedded to a PWM-based grid converter system is presented in Fig. 4. Sampling of the converter currents is synchronized with the PWM and the digital control system is assumed to cause a delay of one sampling period. The DC-bus voltage u_dc is measured for the PWM and the converter current $\boldsymbol{i}_\mathrm{c}$ is controlled by the converter.

A block diagram of the identification algorithm is presented in Fig. 5. While the system is being excited by a wideband excitation signal $\boldsymbol{v}(k)$, the following steps are taken at each sampling period:

A) The most recent samples of the converter voltage reference $\boldsymbol{u}_{\mathrm{c,ref}}$ and the converter current $\boldsymbol{i}_\mathrm{c}$ are input to the algorithm.
B) Significant grid-frequency harmonics, including the fundamental component, are removed from the samples.
C) Parameter estimates of the realistic filter model, $\hat{\boldsymbol{\theta}}_\mathrm{r}$, and the ideal filter model, $\hat{\boldsymbol{\theta}}_\mathrm{i}$, are updated.
D) The estimate $\hat{\boldsymbol{\theta}}_\mathrm{r}$ is translated into an estimate of the series resistance $\hat{R}_\mathrm{s} = \hat{R}_\mathrm{c} + \hat{R}_\mathrm{g}$ and the estimate $\hat{\boldsymbol{\theta}}_\mathrm{i}$ is translated into inductance and capacitance estimates $\hat{L}_\mathrm{c}$, $\hat{C}_\mathrm{f}$, and $\hat{L}_\mathrm{g}$.

These steps are explained in the following subsections.

A. Excitation and Sampling

During identification, an excitation signal $\boldsymbol{v}(k) = v_\alpha(k) + \mathrm{j}v_\beta(k)$ is added to the converter voltage reference calculated by the converter control system, as shown in Fig. 4. In order to successfully identify the LCL filter, the power spectrum of the excitation signal should be wide enough to excite the resonance frequency (7) of the LCL filter sufficiently. Furthermore, the power of the injected signal affects the accuracy of the estimates. Higher power improves the signal-to-noise ratio of the identification, which improves the accuracy of the obtained estimates. A maximum-length binary sequence (MLBS) is used as the excitation signal due to its ease of implementation, deterministic behavior, repeatability, wide power spectrum, and lowest possible crest factor [21], [23]. In this paper, the MLBS is injected into v_β while $v_\alpha = 0$. As a result, only the *b* and *c* phases are excited and thus only the imaginary components of the sampled signals are processed. The choice of amplitude of the MLBS signal is a compromise between excitation power and distortion of the grid currents. Standards, such as the IEEE 519-2014, set limits to harmonics injected to the grid. Compliance with standards solely related to harmonics is not an issue for the proposed method due to the power of the excitation signal spreading mostly to the interharmonic frequencies. However, standards for distributed generation, such as the IEEE 1547-2018, set limits to the total current distortion at the point of connection. The compliance of the proposed method with regards to these standards will be examined in Section V-D.

B. Harmonic Removal

In practice, the grid voltage includes some low-order harmonics in addition to its fundamental component. In order to increase the accuracy of the parameter estimates obtained from the method, significant grid-frequency harmonics should be removed from the current and voltage samples to eliminate the effect of the grid voltage on the estimates. The selected harmonic components are removed from the samples as

$$u(k) = u_{c\beta,\mathrm{ref}}(k) - \sum_m u_m(k) \tag{16}$$

$$i(k) = i_{c\beta}(k) - \sum_m i_m(k) \tag{17}$$

where u_m and i_m are the mth-order harmonics for the voltage and current, respectively. In this paper, the harmonic components $m = [0, 1, 5, 7]$ are removed from the samples. As a result, the sum in (16) becomes $\sum_m u_m(k) = u_0(k) + u_1(k) + u_5(k) + u_7(k)$ and the sum in (17) can be written similarly. The DC component $m = 0$ is removed due to a possible bias in the measurement sensors. Assuming that the grid voltage consists purely of the aforementioned harmonics, its influence is effectively removed from the samples used in the identification. In practice, the grid voltage includes several other frequency components as well. However, these components are typically minor as compared to the low-order grid-frequency harmonics that are removed from the samples. As a result, they are mostly modeled by the noise term $e(k)$.

There are several different algorithms for computing harmonic components from a signal, the standard method for batch processes being the discrete Fourier transform (DFT). The DFT of a signal, e.g., current i, calculated from N previous samples at time k for a mth-order harmonic can be expressed as

$$\boldsymbol{I}_m(k) = \sum_{n=0}^{N-1} i(q+n)\boldsymbol{W}_N^{-mn}, \quad \forall\, m \in \{0, 1, \ldots, N-1\} \tag{18}$$

where $q = k - N + 1$ and $\boldsymbol{W}_N = \mathrm{e}^{\mathrm{j}2\pi/N}$ [24].

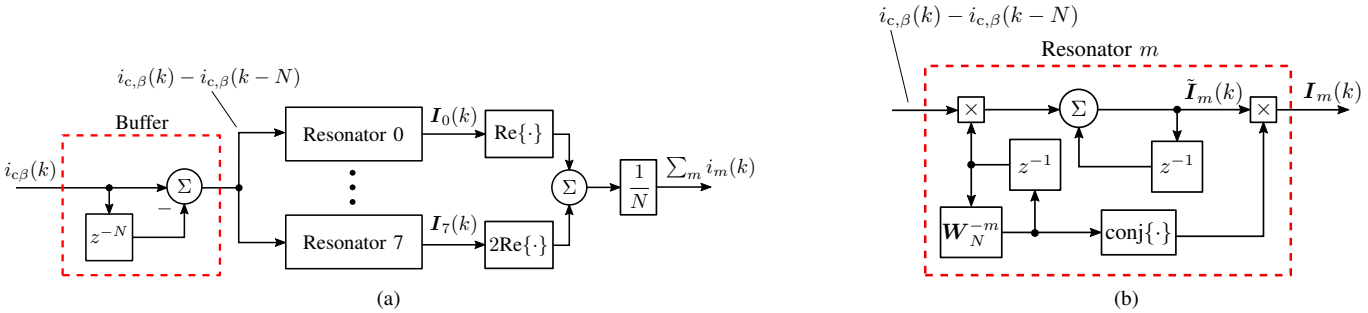

Fig. 6. a) Block diagram representation of the mSDFT algorithm for tracking harmonics $m = [0, 1, 5, 7]$, i.e., the output consists of four frequency components $\sum_m i_m(k) = i_0(k) + i_1(k) + i_5(k) + i_7(k)$. b) Block diagram depicting a single resonator for harmonic m.

For computing a limited number of harmonics efficiently in real time on a sample-to-sample basis, sliding DFT (SDFT) algorithms are a superior tool. The SDFT algorithms leverage the fact that only one element in the sample buffer changes between the sampling instants by modifying the result of the DFT from the previous sampling instant accordingly. The traditional SDFT can be derived from (18) as [25]

$$\boldsymbol{I}_m(k) = \boldsymbol{W}_N^{-mn}\left[\boldsymbol{I}_m(k-1) + i(k) - i(k-N)\right] \tag{19}$$

where $n = \mathrm{mod}(k, N)$. However, this form of the SDFT suffers from numerical instabilities and accumulated errors due to a complex pole on the unit circle [26]. Hence, a guaranteed stable and accurate variant of the sliding DFT, the modulated sliding DFT (mSDFT), is used instead [26]. The structure of the mSDFT is presented in Fig. 6, which depicts the extraction of the harmonics from the converter current samples used in the identification. The mSDFT consists of a comb filter acting as a sample buffer and one resonator for tracking each harmonic of interest. Mathematically, N-point mSDFT of a signal, e.g., current i, at time k for a mth-order harmonic can be expressed as [26]

$$\tilde{\boldsymbol{I}}_m(k) = \tilde{\boldsymbol{I}}_m(k-1) + \boldsymbol{W}_N^{-mn}\left[i(k) - i(k-N)\right] \tag{20}$$

$$\boldsymbol{I}_m(k) = \boldsymbol{W}_N^{m(n+1)}\tilde{\boldsymbol{I}}_m(k) \tag{21}$$

where the tilde indicates that the DFT bin calculated in (20) has phase error that is corrected with (21). Finally, as shown in Fig. 6(a), the spectral bins are transformed into instantaneous values of the harmonics as

$$i_m(k) = \begin{cases} \frac{1}{N}\mathrm{Re}\{\boldsymbol{I}_m(k)\} & \text{if } m = 0 \\ \frac{2}{N}\mathrm{Re}\{\boldsymbol{I}_m(k)\} & \text{otherwise.} \end{cases} \tag{22}$$

C. Model Parameter Estimation

A recursive prediction error (RPE) algorithm [22] is used for computing estimates for the coefficients of the polynomials $A(z)$ and $B(z)$ of the ARMAX model (cf. Appendix B). Estimates for the noise polynomial coefficients $\hat{c}_1$ and $\hat{c}_2$ are also obtained in the process.

For tracking time-varying parameters with the RPE algorithm, either a forgetting factor λ less than unity needs to be used or the covariance matrix $\mathbf{P}$ needs to be actively modified. If neither of these modifications is employed, the tracking capability of time-varying parameters is severely hindered due to the covariance wind-up phenomenon [27]. In the covariance wind-up, the values of a number of elements in the covariance matrix tend to zero, causing the estimation algorithm to become insensitive to certain parameter changes. In [20], two different methods to enable tracking of time-varying parameters were presented. Here, only the constant forgetting factor is considered.

If a forgetting factor less than unity is used, i.e., $\lambda < 1$, the elements of the covariance matrix $\mathbf{P}$ are prevented from tending to zero. The choice of the forgetting factor is a trade-off between sensitivity to disturbances and capability to track parameter variations. The smaller the forgetting factor is, the more aware the estimation algorithm becomes of parameter variations. However, as the sensitivity to parameter changes increases, so does the sensitivity to disturbances. Thus, feasible values for the forgetting factor are often limited close to unity, typically between 0.98 and 0.995 [21].

In estimating the realistic filter model, lower frequencies are given more weight in the estimator by low-pass filtering the samples input to the RPE algorithm (cf. Fig. 5). This improves the accuracy of the estimated model at lower frequencies at the cost of decreasing the accuracy at higher frequencies [22]. For filtering, a simple first-order low-pass filter (LPF) with the bandwidth of $\alpha_\mathrm{f} = 2$ kHz was employed. The choice of the LPF bandwidth α_f is a trade-off between accuracy of the identified series resistance and the accuracy of the high-frequency behavior of the LCL filter. For the system used in the experiments, the bandwidth of 2 kHz was found to be a good compromise between the two. In case the frequency response of the system for a wide range of frequencies is desired, the LPF bandwidth should be maintained relatively high. On the other hand, if only the series resistance is of interest, low LPF bandwidth should be employed. Generally, the frequency range of interest in identification depends on the use case of the estimation result.

D. Translation to Inductance, Capacitance, and Resistance Values

Finally, depending on the identified discrete-time model, the model parameter estimates are translated either into inductance and capacitance values or into series resistance seen by the converter. In the following, the dependency on time k is omitted to maintain a level of simplicity.

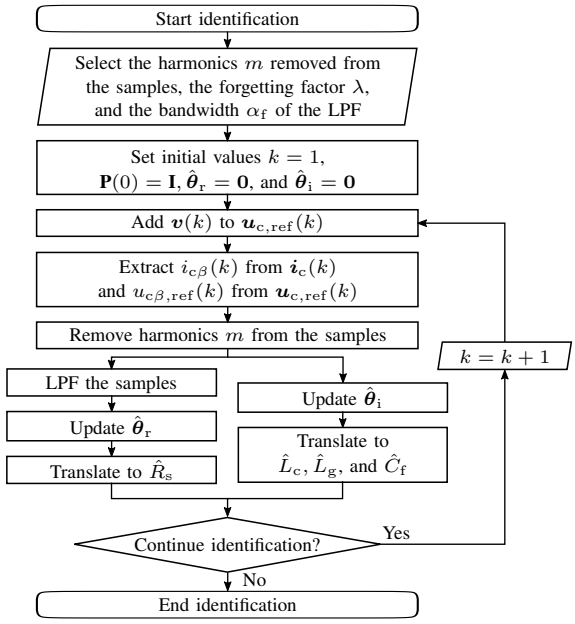

Fig. 7. Flowchart of the identification algorithm.

In case the realistic filter model is identified, the series resistance estimate $\hat{R}_s$, consisting of the estimated converter-side and grid-side resistances $\hat{R}_c$ and $\hat{R}_g$, respectively, is obtained as the inverse of the DC-gain of the identified model, i.e.,

$$\hat{R}_s = \frac{\hat{A}(1)}{\hat{B}(1)} = \frac{1 + \hat{\alpha}_1 + \hat{\alpha}_2 + \hat{\alpha}_3}{\hat{\beta}_1 + \hat{\beta}_2 + \hat{\beta}_3}. \tag{23}$$

In case the ideal filter model is identified, the inductance and capacitance values are obtained by expressing the parameters L_c, C_f, and L_g as functions of the discrete-time model parameters in (6) as [17]

$$\begin{aligned}
\hat{\omega}_p &= \frac{1}{T_s}\cos^{-1}\left(-\frac{\hat{\alpha}_1 + 1}{2}\right) \\
\hat{L}_c &= \frac{2\frac{\sin(\hat{\omega}_p T_s)}{\hat{\omega}_p}[\cos(\hat{\omega}_p T_s) - 1]}{2\hat{\beta}_1\left[\cos(\hat{\omega}_p T_s) - \frac{\sin(\hat{\omega}_p T_s)}{\hat{\omega}_p T_s}\right] + \hat{\beta}_2\left[1 - \frac{\sin(\hat{\omega}_p T_s)}{\hat{\omega}_p T_s}\right]} \\
\hat{L}_g &= -\frac{\hat{\omega}_p \hat{L}_c[\hat{L}_c\hat{\beta}_2 + 2T_s\cos(\hat{\omega}_p T_s)]}{\hat{\omega}_p \hat{L}_c\hat{\beta}_2 + 2\sin(\hat{\omega}_p T_s)} \\
\hat{C}_f &= \frac{\hat{L}_c + \hat{L}_g}{\hat{\omega}_p^2 \hat{L}_c \hat{L}_g}.
\end{aligned} \tag{24}$$

The above equations can either be calculated every sampling period or more sparsely. To summarize, a flowchart of the identification algorithm is shown in Fig. 7.

V. Results

The proposed identification method (cf. Figs. 5 and 7) is evaluated by means of simulations and experiments using a 50-Hz 12.5-kVA grid converter system. During the identification, the converter is controlled using a state-feedback current controller [5] tuned according to Appendix C. The switching frequency of the converter is 5 kHz and the sampling frequency is 10 kHz. An MLBS generated with 9 shift registers

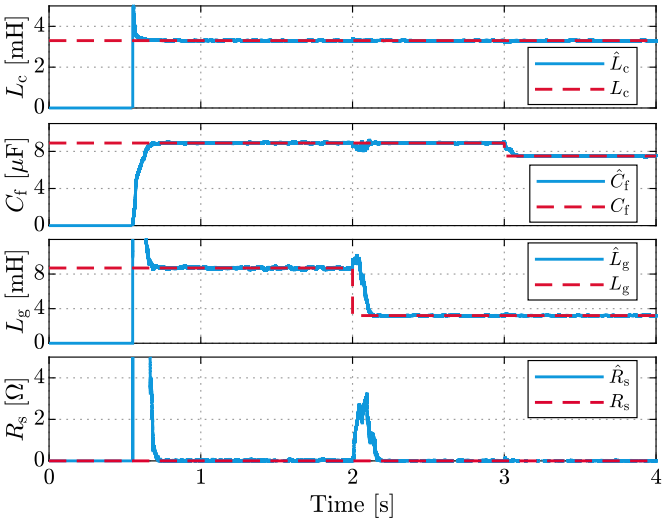

Fig. 8. Simulated evolution of the LCL filter parameter estimates assuming an ideal system. The identification algorithm is initiated at $t = 0.55$ s and two stepwise changes occur: from 8.7 mH to 3.2 mH in the grid-side inductance L_g at $t = 2$ s; from 8.9 µF to 7.5 µF in the filter capacitance C_f at $t = 3$ s.

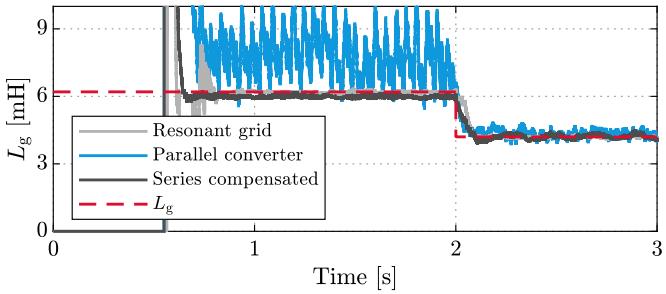

Fig. 9. Simulated evolution of the grid-side inductance estimate under different violations of the inductive-resistive grid assumption. The identification algorithm is initiated at $t = 0.55$ s and a step-wise change of 2 mH occurs in the grid-side inductance L_g at $t = 2$ s.

is used [23]. The amplitude of the MLBS is selected as ± 0.1 p.u. and it is generated at a frequency equal to the sampling frequency. The converter is operating under constant load of 0.4 p.u. The base value of voltage is $\sqrt{2/3} \cdot 400$ V and the base value of current is $\sqrt{2} \cdot 18$ A. The length of the mSDFT buffer is selected as $N = 200$ to match the lowest trackable harmonic frequency with the fundamental frequency of the grid voltage. The initial values of the mSDFT sample buffer are set to zero. A forgetting factor of $\lambda = 0.995$ is used in all of the presented results. In the following, both the realistic and ideal models are estimated in parallel to yield estimates for L_c, C_f, L_g, and R_s. However, it is possible to estimate only one of the models. Unless otherwise stated, the nominal values of the LCL filter reactive parameters are $L_c = 3.3$ mH, $C_f = 8.9$ µF, and $L_{fg} = 3.2$ mH.

A. Simulation: Validating the Proposed Identification Method

A simulation model of the system shown in Fig. 4 was built in Simulink for validating the presented method. PLECS blockset was used to model the physical system in Simulink. Initially, no grid harmonics or losses of either the filter components or the grid are included in the model. For validation, the PWM is modeled as a zero-order hold as assumed in the

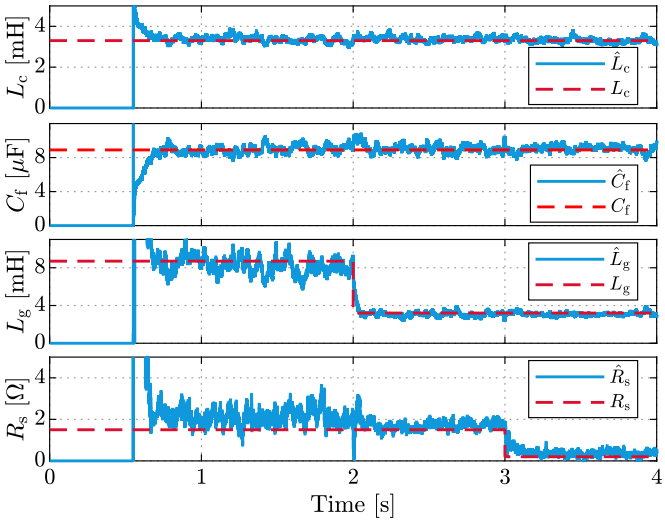

Fig. 10. Simulated evolution of the LCL filter parameter estimates. The identification algorithm is initiated at $t = 0.55$ s and two stepwise changes occur: from 8.7 mH to 3.2 mH in the grid-side inductance L_g at $t = 2$ s; from 1.5 Ω to 0.2 Ω in the grid-side resistance R_g at $t = 3$ s.

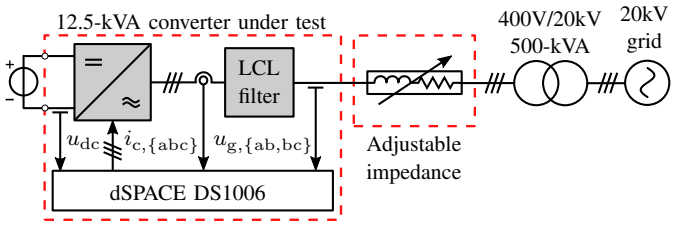

Fig. 11. Block diagram of the experimental setup.

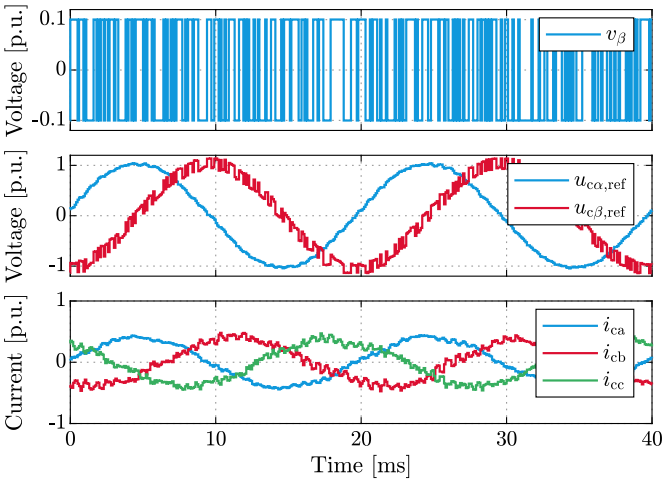

Fig. 12. Measured MLBS excitation signal (first), the space-vector components of the converter voltage reference (second), and the converter phase currents (third).

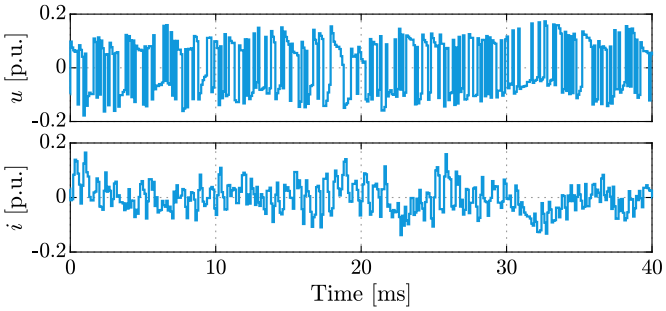

Fig. 13. Sequences of preprocessed voltage u (first) and current i (second) used in the RPE method.

system model. Some noise is assumed in the identification model (8), and thus white noise with standard deviation of 0.002 p.u. is included in the current and voltage measurements. A simulation case using the aforementioned model is presented in Fig. 8. The identification algorithm is initiated at $t = 0.55$ s. In the figure, a stepwise change of grid-side inductance L_g from 8.7 mH to 3.2 mH occurs at $t = 2$ s and a similar stepwise change of filter capacitance C_f from 8.9 μF to 7.5 μF occurs at $t = 3$ s. The nominal values of the estimated parameters are given by the red dashed lines. While the parameters remain constant and the estimation is not in a transient state, the average relative errors of the estimates with respect to their nominal values are all 0%.

B. Simulations: Violating the Assumption of Inductive-Resistive Grid Impedance

Additionally, the effect of violating the assumption of inductive-resistive grid was investigated. In total, three different cases were simulated. Due to space constraints, only the grid-side inductance estimates are shown. As in the previous subsection, all the resistances are assumed zero. The LCL filter reactive parameters are as defined by default ($L_c = 3.3$ mH, $C_f = 8.9$ μF, and $L_{fg} = 3.2$ mH). In the simulations presented for all of the three cases, the total grid inductance L_{gr} is initially 3 mH, i.e., $L_g = L_{fg} + L_{gr} = 6.2$ mH. At $t = 1$ s, the grid inductance L_{gr} drops to 1 mH, i.e., $L_g = 4.2$ mH.

1) High-Frequency Grid Resonances: First, the grid was assumed to have resonant characteristics at higher frequencies. For this, the grid beyond the point of common coupling (PCC) was assumed to be of LCL-type (cf. Fig. 1) without any resistive components. Several different resonance frequencies, ranging from 1 kHz to 22.5 kHz, were simulated. It was found that for grid resonances below the Nyquist frequency of the converter (5 kHz), all of the estimates obtained from the method may be erroneous. However, as the resonance frequency increases, the estimates become increasingly reliable. For grid resonances above the Nyquist frequency, the estimates are hardly affected. The estimate of the grid-side inductance in the case of grid resonance at 6 kHz is shown in Fig. 9. The 2 mH drop in the grid inductance occurs beyond the grid capacitance. Thus, the applicability of the proposed method is limited in grids with resonances below the Nyquist frequency of the converter.

2) Another Converter Connected in Parallel to the PCC: Next, an identical converter was connected in parallel with the identifying converter. The estimate of the grid-side inductance under these conditions is shown in Fig. 9. As can be observed, when the grid impedance is high, most of the excitation flows to the parallel converter, causing distortion in the estimate. The estimates of the resistance R_s and the filter capacitance C_f are distorted similarly while the estimate of the converter-side inductance L_c is unaffected. However, for strong grids, the

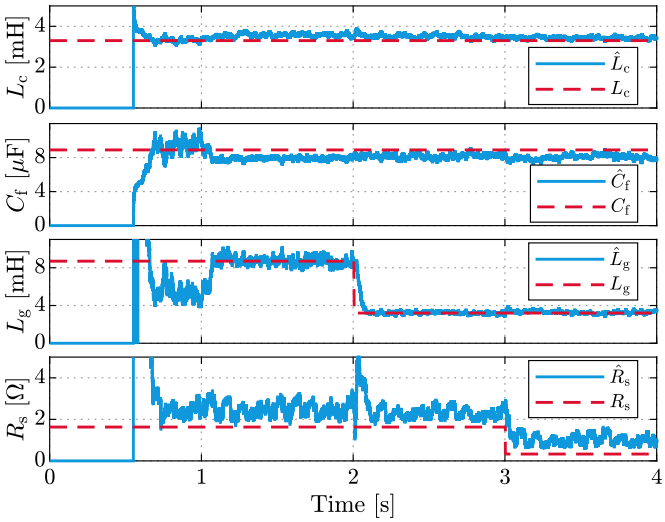

Fig. 14. Experimental evolution of the LCL filter parameter estimates. The identification algorithm is initiated at $t = 0.55$ s and two stepwise changes occur: a relative change of 5.5 mH in the grid-side inductance L_g at $t = 2$ s; a relative change of 1.3 Ω in the grid-side resistance R_g at $t = 3$ s.

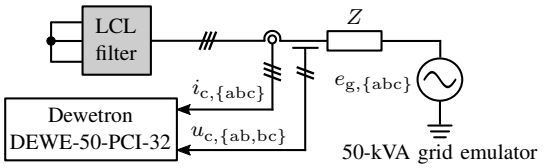

Fig. 15. Block diagram of the LCL filter open-loop frequency response measurement setup.

effect of the parallel converter is lesser. Thus, the applicability of this method is limited for parallel-connected converters in weak grids.

3) Series-Compensated Transmission Line: Lastly, the grid beyond the PCC was assumed to be a series-compensated line, i.e., consisting of a series capacitance and an inductance. The compensation factor is assumed to be $k_c = X_C/X_L = 0.5$, where X_C is the capacitive reactance and X_L is the inductive reactance. The estimate of the grid-side inductance under the aforementioned conditions is shown in Fig. 9. The series-compensation capacitance of 6.7 mF remains constant while the grid inductance changes. As can be observed, the series compensation of the transmission lines has an insignificant effect on the estimate. The estimates of converter-side inductance L_c and filter capacitance C_f are unaffected as well. However, a small low-frequency oscillation is present in the estimate of the series resistance R_s. This is because the series compensation only affects the grid characteristics below and around the fundamental frequency while the grid remains inductive for higher frequencies.

C. Simulation: Stepwise Change in the Grid-side Inductance and Resistance

The simulation model was modified to include grid harmonics, inductor losses, and grid resistance. The grid harmonics consist of 5th and 7th harmonics and both have an amplitude of 0.05 p.u. The filter inductors are modeled to include the effects of DC resistance and eddy currents. Therefore, they

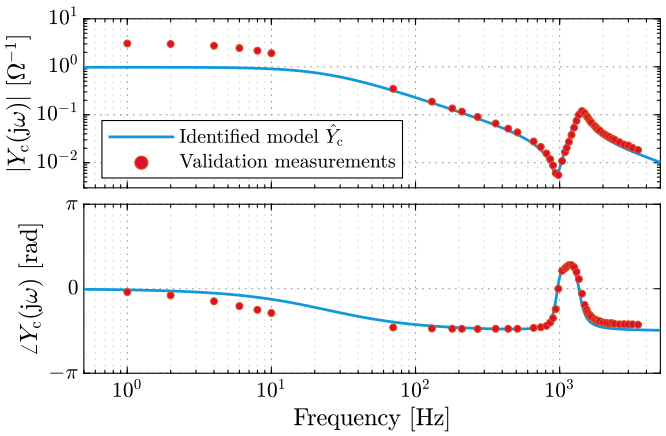

Fig. 16. Identified frequency response of $Y_c(s)$ compared to the measured frequency response of the LCL filter. Both frequency responses are obtained from the same operating point.

TABLE I
NUMBER OF OPERATIONS TO UPDATE THE PARAMETER ESTIMATES

	Multiplications	Additions	Divisions
mSDFT	40	25	0
RPE	101	71	1
Translation to physical parameters	18	8	1
Total	159	104	2

are modeled as an inductance in parallel with a resistance and a resistance in series with the parallel connection of the resistance and the inductance [17]. For the converter-side inductor, the resistance value for the series resistor is $R_c = 100$ mΩ and for the parallel resistor $R_{c,p} = 420$ Ω. Similarly for the grid-side inductor, $R_g = 100$ mΩ and $R_{g,p} = 630$ Ω. A 1.3 Ω resistance is initially included in the grid-side series resistance, i.e., $R_g = 1.4$ Ω. Thus, the total series resistance seen by the converter is initially $R_s = R_c + R_g = 1.5$ Ω. The series resistance R_f of the filter capacitor is set to 5 mΩ. Measurement noise with standard deviation of 0.02 p.u. is added to the current and voltage measurements.

The evolution of the parameter estimates is presented in Fig. 10. In the figure, a stepwise change in the grid-side inductance L_g from 8.7 mH to 3.2 mH occurs at $t = 2$ s, and a stepwise change in the grid-side resistance R_g from 1.5 Ω to 0.2 Ω at $t = 3$ s. After the stepwise parameter changes, the average relative errors of the parameter estimates with respect to their nominal values are 3% for $\hat{L}_c$, 3% for $\hat{C}_f$, and 5% for $\hat{L}_g$. Furthermore, the half-second average value for the estimate of the series resistance R_s is 0.35 Ω. Out of the added non-idealities, the increased measurement noise induces the greatest error to the parameter estimates while the effect of grid harmonics is roughly 0%. The filter inductor resistances cause relative errors of 1% on the inductance estimates.

D. Experiment: Stepwise Change in the Grid-side Inductance and Resistance

The estimation case presented in Fig. 10 is repeated experimentally with a system depicted by the block diagram

in Fig. 11. The converter under test is connected to a 20 kV grid through a 500-kVA 400-V/20-kV transformer and an adjustable impedance. The converter is controlled using a dSPACE DS1006 processor board. The DC-bus voltage, converter currents, and PCC voltages are measured. The PCC voltages are used only in the control system. Stepwise changes in the grid-side inductance and resistance are created by bypassing inductors and resistors with a switch. Fig. 12 shows the injected MLBS excitation v_β, the converter voltage reference components $u_{\mathrm{c}\alpha,\mathrm{ref}}$ and $u_{\mathrm{c}\beta,\mathrm{ref}}$, and the converter phase currents $i_{\mathrm{c,abc}}$, when the MLBS is active. Fig. 13 shows the preprocessed current and voltage sequences i and u from which the grid-frequency harmonics $m = [0, 1, 5, 7]$ have been removed from. These current and voltage sequences are used as an input to the RPE algorithm. Under constant load of 1 p.u. with the excitation applied, the total harmonic distortion (THD), calculated according to IEEE 519-2014, of the first 50 harmonics injected to the grid is approximately 3.9% for a-phase, 5.0% for b-phase, and 5.1% for c-phase. Thus, the THD during identification practically complies with the limit (5%) set by IEEE 519-2014. The total rated current distortion (TRD), calculated according to IEEE 1547-2018, is approximately 4.6% for a-phase, 8.3% for b-phase, and 8.1% for c-phase. To comply with the standard, the amplitude of the excitation could be reduced and the identification could be run intermittently to reduce the average TRD below the limit defined in the standard.

The evolution of the parameter estimates are presented in Fig. 14. In the figure, a stepwise change of 5.5 mH occurs in the grid-side inductance L_{g} at $t = 2$ s, and a stepwise change of $1.3\ \Omega$ occurs in the grid-side resistance R_{g} at $t = 3$ s. After the stepwise changes of the grid-side inductance and resistance, the average relative errors of the parameter estimates with respect to their nominal values are 4% for $\hat{L}_{\mathrm{c}}$, 8% for $\hat{C}_{\mathrm{f}}$, and 3% for $\hat{L}_{\mathrm{g}}$. The reference value for the series resistance seen by the converter is biased, as it does not include the resistive behavior of the converter or the grid. The difference between the half-second averages of the resistance estimates before and after the stepwise change is $1.35\ \Omega$, which is close to the nominal change of $1.3\ \Omega$.

To further validate the proposed method, the estimated pulse-transfer function of the system (5) was formed based on the half-second averages of the estimated model coefficients $\hat{\boldsymbol{\theta}}_{\mathrm{r}}$ of the realistic LCL filter. The estimated pulse-transfer function $\hat{Y}(z)$ was then transformed into $\hat{Y}_{\mathrm{c}}(z)$ by multiplication with the forward-shift operator z, i.e., $\hat{Y}_{\mathrm{c}}(z) = z\hat{Y}(z)$, and finally converted into the s-domain equivalent transfer function $\hat{Y}_{\mathrm{c}}(s)$. The frequency response of $\hat{Y}_{\mathrm{c}}(s)$ was compared to the corresponding experimentally measured open-loop frequency response of the LCL filter. The measurement setup to obtain the open-loop frequency response of the LCL filter is shown in Fig. 15. The grid-side input terminal of the filter was short circuited while the filter was excited with a 50-kVA grid emulator (Regatron TopCon TC.ACS) through an external impedance. The voltages and currents used to calculate the frequency response of the filter were measured at the input terminals of the filter with a data acquisition device (Dewetron DEWE-50-PCI-32) employing a sampling frequency of 100 kHz. The operating point of the filter was set to correspond to that used in the experiments. The comparison of the frequency response of the identified transfer function $\hat{Y}_{\mathrm{c}}(s)$ obtained from the proposed method and the measured open-loop filter frequency response is shown in Fig. 16. Overall, the identified model agrees with the measured open-loop frequency response. The difference in the magnitude at low frequencies is partly due to the bias in the DC gain of the identified system and partly due to the fact that the validation measurements do not contain the effect of the converter parasitic resistances or the grid resistance, which are included in the identified system. However, as seen in Fig. 14, the identification method can accurately track relative changes in the series resistance $\hat{R}_{\mathrm{s}}$ corresponding to the DC gain of $\hat{Y}_{\mathrm{c}}(s)$.

As the estimation result obtained from the ideal simulation model shows (cf. Fig. 8), the identification method yields exact estimates in an ideal case. Therefore, the estimation errors in the experiments are caused by unmodeled dynamics, nonlinearities of the system, unbalances in the filter components, and inaccuracies in the transfer characteristics of the actuator and the measurement devices, as also seen in the simulations including some of these non-idealities (cf. Fig. 10).

E. Computational Aspects of the Proposed Method

Regarding the feasibility of the real-time implementation, Table I shows the number of multiplications, additions, and divisions executed at each sampling period to update the reactive filter parameter estimates. In the table, the harmonics $m = [0, 1, 5, 7]$ are assumed to be removed from the samples. By comparing the number of floating point operations required to update the estimates, around $3 \cdot 10^2$, to the roughly 10^4 operations required in [19], the benefits of the proposed method become evident. The computational burden of the mSDFT can be further alleviated at the cost of increased memory consumption by precomputing the coefficients $\boldsymbol{W}_N^{-mn}$ for each m and $n = \{0, 1, 2, \ldots, N\}$ [26].

VI. Conclusions

This paper presented a real-time identification method for the inductance and capacitance values of LCL filters used in grid converters and the series resistance seen by the converter. The method indirectly estimates the grid inductance as a part of the grid-side inductance of the LCL filter. As a result, the parameters of an inductive-resistive grid can be obtained indirectly. The presented method can be embedded to a control system of PWM-based converters in a plug-in manner. An SDFT algorithm is used for computing the grid-frequency harmonics to enable computationally efficient real-time harmonic computation. A single recursive parameter estimation algorithm is used to estimate the identification model parameters. A forgetting factor is employed in the recursive parameter estimation algorithm to enable tracking of time-varying parameters. Simulation and experimental results show that the method converges to correct estimates from its initial state and it is capable of tracking time-varying LCL filter parameters with good accuracy.

APPENDIX A
DISCRETE-TIME MODEL OF THE LCL FILTER

A discrete-time model of an LCL filter in stationary coordinates is presented below. The state vector is selected as $\mathbf{x} = [\boldsymbol{i}_\mathrm{c}, \boldsymbol{u}_\mathrm{f}, \boldsymbol{i}_\mathrm{g}]^\mathrm{T}$. The sampling of the converter currents and grid voltages is synchronized with the PWM, which is modeled as a zero-order hold. Under these assumptions, the system matrix $\boldsymbol{\Phi}$ and the input vector $\boldsymbol{\Gamma}_\mathrm{c}$ required for solving $Y_\mathrm{c}(z)$ are obtained from [28]

$$\boldsymbol{\Phi} = \mathrm{e}^{\mathbf{A}T_\mathrm{s}} \qquad \boldsymbol{\Gamma}_\mathrm{c} = \left(\int_0^{T_\mathrm{s}} \mathrm{e}^{\mathbf{A}\tau} \mathrm{d}\tau \right) \mathbf{B}_\mathrm{c} \tag{25}$$

where

$$\mathbf{A} = \begin{bmatrix} -\frac{R_\mathrm{c}+R_\mathrm{f}}{L_\mathrm{c}} & -\frac{1}{L_\mathrm{c}} & \frac{R_\mathrm{f}}{L_\mathrm{c}} \\ \frac{1}{C_\mathrm{f}} & 0 & -\frac{1}{C_\mathrm{f}} \\ \frac{R_\mathrm{f}}{L_\mathrm{g}} & \frac{1}{L_\mathrm{g}} & -\frac{R_\mathrm{f}+R_\mathrm{g}}{L_\mathrm{g}} \end{bmatrix} \qquad \mathbf{B}_\mathrm{c} = \begin{bmatrix} \frac{1}{L_\mathrm{c}} \\ 0 \\ 0 \end{bmatrix} \tag{26}$$

are the corresponding continuous-time counterparts of the system matrix and the input vector for the converter voltage, respectively. The input vector $\boldsymbol{\Gamma}_\mathrm{g}$ can be obtained similarly to $\boldsymbol{\Gamma}_\mathrm{c}$.

In the case of an ideal LCL filter, i.e., when the resistances are omitted, the closed-form expressions for the system matrix $\boldsymbol{\Phi}$ and the input vector $\boldsymbol{\Gamma}_\mathrm{c}$ become

$$\boldsymbol{\Phi} = \begin{bmatrix} \frac{L_\mathrm{c}+L_\mathrm{g}\cos(\omega_\mathrm{p}T_\mathrm{s})}{L_\mathrm{c}+L_\mathrm{g}} & -\frac{\sin(\omega_\mathrm{p}T_\mathrm{s})}{\omega_\mathrm{p}L_\mathrm{c}} & \frac{L_\mathrm{g}[1-\cos(\omega_\mathrm{p}T_\mathrm{s})]}{L_\mathrm{c}+L_\mathrm{g}} \\ \frac{\sin(\omega_\mathrm{p}T_\mathrm{s})}{\omega_\mathrm{p}C_\mathrm{f}} & \cos(\omega_\mathrm{p}T_\mathrm{s}) & -\frac{\sin(\omega_\mathrm{p}T_\mathrm{s})}{\omega_\mathrm{p}C_\mathrm{f}} \\ \frac{L_\mathrm{c}[1-\cos(\omega_\mathrm{p}T_\mathrm{s})]}{L_\mathrm{c}+L_\mathrm{g}} & \frac{\sin(\omega_\mathrm{p}T_\mathrm{s})}{\omega_\mathrm{p}L_\mathrm{g}} & \frac{L_\mathrm{g}+L_\mathrm{c}\cos(\omega_\mathrm{p}T_\mathrm{s})}{L_\mathrm{c}+L_\mathrm{g}} \end{bmatrix} \tag{27}$$

and

$$\boldsymbol{\Gamma}_\mathrm{c} = \frac{1}{L_\mathrm{c}+L_\mathrm{g}} \begin{bmatrix} T_\mathrm{s} + \frac{L_\mathrm{g}\sin(\omega_\mathrm{p}T_\mathrm{s})}{\omega_\mathrm{p}L_\mathrm{c}} \\ L_\mathrm{g}[1-\cos(\omega_\mathrm{p}T_\mathrm{s})] \\ T_\mathrm{s} - \frac{\sin(\omega_\mathrm{p}T_\mathrm{s})}{\omega_\mathrm{p}} \end{bmatrix}. \tag{28}$$

APPENDIX B
RECURSIVE PREDICTION ERROR METHOD

The RPE algorithm [22] is presented below. It calculates an estimate $\hat{\boldsymbol{\theta}}$ based on the prediction error

$$\hat{e}(k) = y(k) - \hat{\boldsymbol{\varphi}}^\mathrm{T}(k)\hat{\boldsymbol{\theta}}(k-1) \tag{29}$$

where $\hat{\boldsymbol{\varphi}}(k)$ is the regressor vector with true noise terms $e(k-1)$ and $e(k-2)$ replaced with their estimated values $\hat{e}(k-1)$ and $\hat{e}(k-2)$, respectively. The parameter vector is estimated recursively as

$$\hat{\boldsymbol{\theta}}(k) = \hat{\boldsymbol{\theta}}(k-1) + \mathbf{K}(k)\hat{e}(k) \tag{30}$$

where the gain $\mathbf{K}$ is calculated as

$$\mathbf{K}(k) = \mathbf{P}(k)\boldsymbol{\psi}(k) = \frac{\mathbf{P}(k-1)\boldsymbol{\psi}(k)}{\lambda + \boldsymbol{\psi}^\mathrm{T}(k)\mathbf{P}(k-1)\boldsymbol{\psi}(k)} \tag{31}$$

$$\mathbf{P}(k) = \frac{\mathbf{P}(k-1)}{\lambda} - \frac{\mathbf{P}(k-1)\boldsymbol{\psi}(k)\boldsymbol{\psi}^\mathrm{T}(k)\mathbf{P}(k-1)}{\lambda[\lambda + \boldsymbol{\psi}^\mathrm{T}(k)\mathbf{P}(k-1)\boldsymbol{\psi}(k)]} \tag{32}$$

where $\boldsymbol{\psi}(k)$ is an approximate gradient. For the realistic filter model, the approximate gradient is given by

$$\begin{aligned} \boldsymbol{\psi}_\mathrm{r}(k) = [&- i_\mathrm{F}(k-1), -i_\mathrm{F}(k-2), -i_\mathrm{F}(k-3), u_\mathrm{F}(k-2), \\ &u_\mathrm{F}(k-3), u_\mathrm{F}(k-4), \hat{e}_\mathrm{F}(k-1), \hat{e}_\mathrm{F}(k-2)]^\mathrm{T}. \end{aligned} \tag{33}$$

For the ideal filter model, the approximate gradient is given by

$$\begin{aligned} \boldsymbol{\psi}_\mathrm{i}(k) = [&i_\mathrm{F}(k-2) - i_\mathrm{F}(k-1), u_\mathrm{F}(k-2) + u_\mathrm{F}(k-4), \\ &u_\mathrm{F}(k-3), u_\mathrm{F}(k-4), \hat{e}_\mathrm{F}(k-1), \hat{e}_\mathrm{F}(k-2)]^\mathrm{T}. \end{aligned} \tag{34}$$

The elements of the approximate gradients for both (33) and (34) can be solved from

$$\begin{aligned} i_\mathrm{F}(k) &= i(k) - \hat{c}_1(k)i_\mathrm{F}(k-1) - \hat{c}_2(k)i_\mathrm{F}(k-2) \\ u_\mathrm{F}(k) &= u(k) - \hat{c}_1(k)u_\mathrm{F}(k-1) - \hat{c}_2(k)u_\mathrm{F}(k-2) \\ \hat{e}_\mathrm{F}(k) &= \hat{e}(k) - \hat{c}_1(k)\hat{e}_\mathrm{F}(k-1) - \hat{c}_2(k)\hat{e}_\mathrm{F}(k-2). \end{aligned} \tag{35}$$

The equations (29)–(32) are applicable to both the realistic and ideal filter models. Initial values for $\hat{\boldsymbol{\theta}}$ and $\mathbf{P}$ are required in order to start the algorithm. The initial values are $\hat{\boldsymbol{\theta}}(0) = 0$ and $\mathbf{P}(0) = \mathbf{I}$ p.u for both models.

If convergence issues arise due to the nature of the RPE method, a slightly modified version of the method should be used to obtain initial estimates. This modification is accomplished by setting the estimates of the noise polynomials zero, i.e., $\hat{c}_1 = 0$ and $\hat{c}_2 = 0$, in the equations for calculating the approximate gradient (35). After the initial transients in the estimates have subsided, the approximate gradient should be calculated normally according to (35).

APPENDIX C
DESIGN PARAMETERS FOR THE CONTROL METHOD

The parameters for the observer-based current control method of [5] are $\omega_\mathrm{cd} = 2\pi \cdot 150$ rad/s, $\zeta_\mathrm{cd} = 1$, $\omega_\mathrm{cr} = \omega_\mathrm{p}$, $\zeta_\mathrm{cr} = 0.01$, $\omega_\mathrm{od} = 3\omega_\mathrm{cd}$, $\zeta_\mathrm{od} = 1$, $\omega_\mathrm{or} = \omega_\mathrm{p} - \omega_\mathrm{g}$, and $\zeta_\mathrm{or} = 0.7$. The notation follows that used in [5]. The synchronous reference frame of the control system was established using a SRF-PLL tuned with with $\zeta_\mathrm{PLL} = 0.7$ and $\omega_\mathrm{PLL} = 2\pi \cdot 15$ rad/s. The DC-bus voltage is assumed constant.

For direct identification in closed-loop systems, the noise e affects the input signal u [cf. (8)] through the feedback loop and results in biased estimates [21]. The level of bias depends on the accuracy of the selected noise model and on the controller tuning. Therefore, reduced bandwidth and damping factors are used for the duration of the identification to reduce the bias caused by the feedback loop.

REFERENCES

[1] M. Liserre, F. Blaabjerg, and S. Hansen, "Design and control of an LCL-filter-based three-phase active rectifier," *IEEE Trans. Ind. Appl.*, vol. 41, no. 5, pp. 1281–1291, Sep./Oct. 2005.

[2] V. Blasko and V. Kaura, "A novel control to actively damp resonance in input LC filter of a three-phase voltage source converter," *IEEE Trans. Ind. Appl.*, vol. 33, no. 2, pp. 542–550, Mar./Apr. 1997.

[3] C. A. Busada, S. G. Jorge, and J. A. Solsona, "Full-state feedback equivalent controller for active damping in LCL-filtered grid-connected inverters using a reduced number of sensors," *IEEE Trans. Ind. Electron.*, vol. 62, no. 10, pp. 5993–6002, Oct. 2015.

[4] J. Dannehl, F. W. Fuchs, S. Hansen, and P. B. Thogersen, "Investigation of active damping approaches for PI-based current control of grid-connected pulse width modulation converters with LCL filters," *IEEE Trans. Ind. Appl.*, vol. 46, no. 4, pp. 1509–1517, Jul./Aug. 2010.

[5] J. Kukkola, M. Hinkkanen, and K. Zenger, "Observer-based state-space current controller for a grid converter equipped with an LCL filter: Analytical method for direct discrete-time design," *IEEE Trans. Ind. Appl.*, vol. 51, no. 5, pp. 4079–4090, Sep./Oct. 2015.

[6] H. Soliman, H. Wang, and F. Blaabjerg, "A review of the condition monitoring of capacitors in power electronic converters," *IEEE Trans. Ind. Appl.*, vol. 52, no. 6, pp. 4976–4989, Nov./Dec. 2016.

[7] T. Roinila, M. Vilkko, and J. Sun, "Online grid impedance measurement using discrete-interval binary sequence injection," *IEEE Trans. Emerg. Sel. Topics Power Electron.*, vol. 2, no. 4, pp. 985–993, Dec. 2014.

[8] S. Cobreces, E. J. Bueno, D. Pizarro, F. J. Rodriguez, and F. Huerta, "Grid impedance monitoring system for distributed power generation electronic interfaces," *IEEE Trans. Instrum. Meas.*, vol. 58, no. 9, pp. 3112–3121, Sep. 2009.

[9] P. Garcia, M. Sumner, Á. Navarro-Rodríguez, J. M. Guerrero, and J. Garcia, "Observer-based pulsed signal injection for grid impedance estimation in three-phase systems," *IEEE Trans. Ind. Electron.*, vol. 65, no. 10, pp. 7888–7899, Oct. 2018.

[10] D. Pérez-Estévez and J. Doval-Gandoy, "Grid Impedance Identification Using the VSC Switching Ripple," in *Proc. IEEE ECCE*, Baltimore, MD, USA, Sep./Oct. 2019, pp. 1506–1513.

[11] B. Arif, L. Tarisciotti, P. Zanchetta, J. C. Clare, and M. Degano, "Grid parameter estimation using model predictive direct power control," *IEEE Trans. Ind. Appl.*, vol. 51, no. 6, pp. 4614–4622, Nov./Dec. 2015.

[12] N. Hoffmann and F. W. Fuchs, "Minimal invasive equivalent grid impedance estimation in inductive–resistive power networks using extended Kalman filter," *IEEE Trans. Power Electron.*, vol. 29, no. 2, pp. 631–641, Feb. 2014.

[13] D. K. Alves, R. L. Ribeiro, F. B. Costa, and T. O. A. Rocha, "Real-time wavelet-based grid impedance estimation method," *IEEE Trans. Ind. Electron.*, vol. 66, no. 10, pp. 8263–8265, Oct. 2019.

[14] F. Huerta, S. Cobreces, F. J. Rodríguez, D. Pizarro, and F. Meca, "Black-box identification for an auto-tuned current controller working with voltage source converters connected to the grid through a LCL filter," in *Proc. IEEE ISIE*, Bari, Italy, Jul. 2010, pp. 96–101.

[15] F. Huerta, S. Cobreces, F. Rodriguez, M. Moranchel, and I. Sanz, "State-space black-box model identification of a voltage-source converter with LCL filter," in *Proc. IEEE PEDG*, Aalborg, Denmark, Jun. 2012, pp. 550–557.

[16] F. Huerta, S. Cobreces, F. Rodríguez, C. Clancey, and I. Sanz, "Comparison of two black-box model identification methods applied on a VSC with LCL filter," in *Proc. IEEE IECON*, Montreal, Canada, Oct. 2012, pp. 4648–4653.

[17] J. Koppinen, J. Kukkola, and M. Hinkkanen, "Parameter estimation of an LCL filter for control of grid converters," in *Proc. IEEE ICPE-ECCE*, Seoul, South Korea, Jun. 2015, pp. 1260–1267.

[18] ——, "Identification of LCL filter parameters," European Patent 3 096 429 (B1), Dec. 11, 2019.

[19] ——, "Plug-in identification method for an LCL filter of a grid converter," *IEEE Trans. Ind. Electron.*, vol. 65, no. 8, pp. 6270–6280, Aug. 2018.

[20] V. Pirsto, J. Kukkola, F. M. M. Rahman, and M. Hinkkanen, "Real-time identification method for LCL filters used with grid converters," in *Proc. IEEE ECCE*, Baltimore, MD, USA, Sep./Oct. 2019, pp. 3729–3736.

[21] L. Ljung, *System Identification: Theory for the User*, 2nd ed. Troy, NY: Prentice-Hall, 1999.

[22] T. Söderström and P. Stoica, *System Identification*. London, UK: Prentice-Hall, 1989.

[23] T. Roinila, M. Vilkko, and J. Sun, "Broadband methods for online grid impedance measurement," in *Proc. IEEE ECCE*, Denver, CO, USA, Sep. 2013, pp. 3003–3010.

[24] J. G. Proakis and D. K. Manolakis, *Digital Signal Processing*, 4th ed. Upper Saddle River, NJ: Prentice-Hall, Inc., 2006.

[25] E. Jacobsen and R. Lyons, "The sliding DFT," *IEEE Signal. Proc. Mag.*, vol. 20, no. 2, pp. 74–80, Mar. 2003.

[26] K. Duda, "Accurate, guaranteed stable, sliding discrete Fourier transform [DSP tips & tricks]," *IEEE Signal. Proc. Mag.*, vol. 27, no. 6, pp. 124–127, Nov. 2010.

[27] K. J. Åström and B. Wittenmark, *Adaptive Control*, 2nd ed. Boston, MA: Addison-Wesley Longman Publishing Co., Inc., 1994.

[28] G. F. Franklin, J. D. Powell, and M. Workman, *Digital control of dynamic systems*, 3rd ed. Menlo Park, CA: Addison-Wesley, 1998.

Ville Pirsto received the B.Sc. (Tech.) and M.Sc. (Tech.) degrees in electrical engineering from the Aalto University, Espoo, Finland, in 2017 and 2019, respectively, where he is currently working toward the D.Sc. (Tech.) in electrical engineering.

His current research focuses on grid-connected converters.

Jarno Kukkola received the B.Sc. (Tech.), M.Sc. (Tech.), and D.Sc. (Tech.) degrees in electrical engineering from the Aalto University, Espoo, Finland, in 2010, 2012, and 2017, respectively.

He is currently a Postdoctoral Researcher with the School of Electrical Engineering, Aalto University, Espoo, Finland. His research interests include control systems and grid-connected converters.

F. M. Mahafugur Rahman (S'20) received the B.Sc.(Tech.) degree in electrical and electronic engineering from the Chittagong University of Engineering and Technology, Chittagong, Bangladesh, in 2011. He received the M.Sc.(Tech.) degree in electronics and electrical engineering from the Aalto University, Espoo, Finland, in 2016, where he is currently working toward the D.Sc.(Tech.) degree in electrical engineering.

His research interests include control of grid-connected converters.

Marko Hinkkanen (M'06–SM'13) received the M.Sc.(Eng.) and D.Sc.(Tech.) degrees in electrical engineering from the Helsinki University of Technology, Espoo, Finland, in 2000 and 2004, respectively.

He is currently an Associate Professor with the School of Electrical Engineering, Aalto University, Espoo, Finland. His research interests include control systems, electric drives, and power converters.

Dr. Hinkkanen was the corecipient of the 2016 International Conference on Electrical Machines (ICEM) Brian J. Chalmers Best Paper Award, the 2016 and 2018 IEEE Industry Applications Society Industrial Drives Committee Best Paper Awards, and the 2020 SEMIKRON Innovation Award. He is an Associate Editor for the IEEE TRANSACTIONS ON ENERGY CONVERSION and the *IET Electric Power Applications*.